

Cite this: *J. Mater. Chem. C*, 2023, **11**, 5524

On the coexistence of ferroelectric and antiferroelectric polymorphs in NaNbO_3 fibers at room temperature†

Guilhermina Ferreira Teixeira,^a Heitor Secco Seleghini,^b Wagner Benício Bastos,^c Natalia Jacomaci,^d Bojan Stojadinović,^e Zorana Dohčević-Mitrović,^e Flavio Colmati,^a Miguel Angel San-Miguel,^b Elson Longo^c and Maria Aparecida Zaghete^{cf}

$\text{Na}_2\text{Nb}_2\text{O}_6 \cdot \text{H}_2\text{O}$ fibers were synthesized in a short time using a microwave-assisted hydrothermal method and later used as a precursor for obtaining NaNbO_3 fibers with piezoelectric characteristics. The NaNbO_3 fibers consist of a mix of antiferroelectric (*Pbcm*) and ferroelectric (*P2₁ma*) orthorhombic phases. The ferroelectric structure comprises about 87% wt of the sample, and a theoretical approach indicated that an electric field could induce an inversion in the relative stability between the most stable antiferroelectric structure and the ferroelectric one. Piezoresponse force microscopy showed that an individual fiber is composed of regions with ferroelectric domains and regions with no ferroelectric characteristics.

Received 23rd September 2022,
Accepted 22nd March 2023

DOI: 10.1039/d2tc04039e

rsc.li/materials-c

Introduction

Contemporary society has experienced technological development that has led research to focus on materials that have and combine functional properties. Sodium niobate (NaNbO_3) is a multifunctional perovskite-structured material with interesting properties^{1–6} and shows a complex structural phase transition as a function of pressure, temperature, and particle size.^{7–9}

NaNbO_3 shows polymorphism that is yet to be fully understood, and several studies have focused on elucidating its crystalline structures. Depending on the processing route, NaNbO_3 can grow in paraelectric, antiferroelectric, or ferroelectric phases.^{10–13} Although NaNbO_3 exhibits an orthorhombic antiferroelectric phase at room temperature, some studies have reported the ferroelectric phase of the orthorhombic structure under this condition.^{14–16}

Piezoelectricity is one of the most interesting properties of NaNbO_3 , making this compound an environmentally friendly substitute for lead titanate zirconate (PZT ($\text{Pb}(\text{Zr}_{1-x}\text{Ti}_x)\text{O}_3$))¹² ceramics in piezoelectric devices. The piezoelectric effect may be classified as direct or converse. The direct effect consists of creating an electric charge by submitting a material to mechanical stress. In turn, the converse piezoelectric effect occurs by converting electric energy into mechanical stress.¹⁷

Non-centrosymmetric crystals show spontaneous polarization that is an important condition for piezoelectricity to occur; however, nonpolar materials such as zinc oxide (ZnO) with a hexagonal wurtzite crystal structure might also present the piezoelectric effect. This occurs because piezoelectricity is a property with tensorial character, and the piezoelectric tensor may vary according to the crystallographic group.¹⁸

Energy harvesting devices^{19,20} operate based on the piezoelectric effect and the piezoelectric constant of nanomaterials is lower than that of bulk piezoelectric materials. Thus, synthesizing compounds whose characteristics allow increasing the charges generated under certain stress is an important step to improve the piezoelectric behavior of nanostructures. In this sense, the growth of particles with one-dimensional morphology has been a great alternative to enhance the piezoelectric response of a nanomaterial.²¹ This occurs because the elastic coefficient of the piezoelectric particles with one-dimensional morphology decreases, thus increasing the elastic limit and piezoelectric constant along with the lower particle diameter. Thus, the material becomes very sensitive to low-frequency and irregular mechanical

^a Universidade Federal de Goiás, Instituto de Química, Goiânia, GO, Brazil.
E-mail: mina.guilher@gmail.com

^b Unicamp Material Simulation Lab, Institute of Chemistry,
State University of Campinas, Campinas, SP, Brazil

^c CDMF-Universidade Federal de São Carlos, PO Box, 676, 13565-905 São Carlos,
SP, Brazil

^d Renato Archer Information Technology Center, Campinas, SP, Brazil

^e Nanostructured Matter Laboratory, Institute of Physics Belgrade,
University of Belgrade, Pregrevica 118, 11080 Belgrade, Serbia

^f Universidade Estadual Paulista Júlio de Mesquita Filho, Instituto de Química,
Araraquara, SP, Brazil

† Electronic supplementary information (ESI) available. See DOI: <https://doi.org/10.1039/d2tc04039e>

vibration.²¹ Therefore, for energy harvesting applications, it is essential to choose the best route to prepare particles with these characteristics.

Studies that explore one-dimensional perovskite nanostructures for applications in energy harvesting devices have grown.²² Many of them have addressed the one-dimensional NaNbO_3 obtained from the thermal treatment of the $\text{Na}_2\text{Nb}_2\text{O}_6\cdot\text{H}_2\text{O}$ metastable phase synthesized using a hydrothermal method.

Hydrothermal synthesis methods have the advantage of obtaining crystalline particles with different morphologies at low temperatures and relatively short synthesis periods. However, by using microwave radiation as a heating source, the time and temperature to obtaining crystalline particles decrease considerably.²³ Such a variation in hydrothermal synthesis is known as the Microwave-Assisted Hydrothermal Method (MAHM). In a conventional hydrothermal method, orthorhombic NaNbO_3 with the $P2_1ma$ space group is obtained from $\text{Na}_2\text{Nb}_2\text{O}_6\cdot\text{H}_2\text{O}$ synthesized at 200 °C in 4 hours of synthesis, while NaNbO_3 with the $Pbma$ space group is obtained after 24 hours of hydrothermal treatment.¹⁶ Furthermore, using the MAHM, NaNbO_3 ($Pbma$) is obtained at 180 °C in 30 minutes.²⁴

The spontaneous polarization in the non-centrosymmetric orthorhombic $P2_1ma$ phase of NaNbO_3 is a fundamental condition for the particles to present piezoelectric and ferroelectric behaviors.^{14,16,25} Therefore, ensuring the growth of NaNbO_3 in an orthorhombic structure with the $P2_1ma$ space group rather than antiferroelectric symmetries (e.g., $Pbcm$ or $Pbma$) is a significant aspect to consider when aiming to synthesize NaNbO_3 with a piezoelectric response. In this sense, the conventional heating of $\text{Na}_2\text{Nb}_2\text{O}_6\cdot\text{H}_2\text{O}$ synthesized using the hydrothermal method has been a suitable route for obtaining one-dimensional orthorhombic NaNbO_3 with the $P2_1ma$ space group.^{16,25}

Piezoresponse force microscopy (PFM) is a powerful tool for investigating the ferroelectricity of bulk materials, as well as materials at the nanoscale level (nanostructures and thin films).^{26–31} In the last few decades, PFM has allowed comprehensive studies on the processes of electrical polarization and wall dynamics of the ferroelectric domains,^{32,33} switching of polarization and nucleation domains,^{34,35} and the behavior of ferroelectric properties with different parameters in the preparation of materials.^{36–38}

Thus, in this context, this work is a thorough study of the structure of one-dimensional NaNbO_3 based on a set of experimental characterization techniques and an atomistic computational approach. In addition, the piezoresponse force microscopy tool was fundamental to measure the piezoelectric response of individual fibers, unveiling the relationship between the crystalline structure of the fibers and their piezoelectric behavior. The results indicate that the fibers can be applied as piezoelectric materials.

Experimental procedure

NaNbO_3 fiber synthesis

The NaNbO_3 fibers were produced through conventional thermal treatment of $\text{Na}_2\text{Nb}_2\text{O}_6\cdot\text{H}_2\text{O}$ fibers synthesized using the MAHM.

The synthesis of $\text{Na}_2\text{Nb}_2\text{O}_6\cdot\text{H}_2\text{O}$ fibers started with NaOH (p.a. Quemis), which acts as a mineralizer agent and sodium source, Nb_2O_5 (Alfa Aesar, 99%), and PVA (NEON). The reaction was carried out in a Teflon vessel model XP-1500 (CEM-Corp) in a MARS-5 (CEM-Corp.) microwave oven. The precursor suspension was prepared by adding 0.70 g of Nb_2O_5 to 30 mL of a solution containing 0.36 g L⁻¹ of PVA. After 10 minutes of stirring, 10.0 g of NaOH was introduced to the suspension and kept under stirring for 30 minutes. Then, the suspension was transferred to a Teflon vessel and placed inside the microwave oven. The synthesis was carried out at 160 °C for 40 minutes. The product was washed with distilled water through centrifugation until neutralizing pH and then dried at room temperature. After drying, the $\text{Na}_2\text{Nb}_2\text{O}_6\cdot\text{H}_2\text{O}$ product was calcinated at 550 °C for 4 hours in a muffle furnace to produce NaNbO_3 with an anisotropic morphology.

Characterization techniques

The product obtained was characterized through X-ray powder diffraction (XRD) using a Rigaku-DMAX/2500PC diffractometer (Japan) with Cu-K α radiation ($\lambda = 1.5406 \text{ \AA}$) in the 2θ range from 20° to 80° with 0.20° min⁻¹. The Rietveld refinement was performed on the TOPAS Academic (v.5) software. The morphology of the as-prepared samples was observed using a high-resolution field-emission gun scanning electron microscopy FE-SEM system (JEOL, JSM-7500F). The micro-Raman spectra were collected in a backscattering geometry using a TriVista 557 triple spectrometer equipped with a nitrogen-cooled CCD detector. Micro-Raman scattering measurements were performed using a Linkam THMSG600 microscope heating stage in a temperature range between room temperature and 180 K. The 532 nm line of a solid-state Nd:YAG laser was used as an excitation source, with an incident laser power of less than 40 mW to minimize the heating effects and/or sample degradation. The topography, piezo response images, and local piezohysteresis loops in the nanoscale were obtained using a commercial AFM (MultiMode Nanoscope V, Bruker). The AFM system was modified to work as a piezoresponse force microscopy (PFM)³⁹ system using a function generator (33220A, Agilent), a power source (2410C Source Meter, Keithley), and a lock-in amplifier (SR850, Stanford). The sample was prepared by depositing the fibers on a Pt-coated substrate (bottom electrode). For deposition, the fibers were suspended in isopropyl alcohol and dropped onto the substrate. The tip was used as a mobile electrode top. During the piezo response measurements, an external AC electric signal of 1V (RMS) was applied between a conductive probe (PPP-NCHR, Nanosensors, 42 N m⁻¹) and a bottom Pt electrode. Frequencies of 50 kHz and 5 kHz were used to obtain out-of-plane (OP-PFM) and in-plane (IP-PFM) piezo response measurements, respectively. The piezo response image scans were performed with a relative angle of 17° between the cantilever and the NaNbO_3 fiber.

Computational details

We carried out the computational RAMAN and relative stability study based on Density Functional Theory (DFT) calculations^{40,41} using the CRYSTAL17 package version 1.0.2,⁴² which employs Gaussian-type orbitals as basic functions. The basic sets for Na,

Nb, and O were 8-511G, 986-31(631d) G, and 8-411,^{43–45} respectively. The exchange–correlation term was treated with the following three different functionals: PBE,⁴⁶ B3LYP,^{47,48} and HSE06^{49–51} to compare the relative stability between the polymorphs and using only the B3LYP functional for obtaining the vibrational modes. All calculations treated the van der Waals interactions using the D3 semi-empirical dispersion scheme with BJ-damping.^{52–54} The k -points were sampled through the Monkhorst–Pack method with a $5 \times 5 \times 5$ mesh.⁵⁵ Since it is necessary to use standard space groups for input in the CRYSTAL17 package, the $P2_1ma$ space group was treated as the standard $Pmc2_1$ space group. The vibrational modes at the G -point were obtained according to the FREQCAL routine implemented in CRYSTAL17, and the analytical RAMAN intensities were obtained using the coupled perturbed Hartree–Fock method^{56,57} with a simulated laser irradiation frequency of 532 nm and a simulated temperature of 295 K. We performed the simulated application of an external electric field to the polymorphs using the finite-field approach (FIELD-tag)⁵⁸ with 60 Fourier terms for the triangular-form potential expansion. Due to the computational cost, the Monkhorst–Pack k -points mesh was reduced to $4 \times 4 \times 4$.

Results and discussion

As the metastable $\text{Na}_2\text{Nb}_2\text{O}_6 \cdot \text{H}_2\text{O}$ is normally used as a precursor of NaNbO_3 anisotropic particles, we employed microwaves as a heating source to accelerate the process of obtaining $\text{Na}_2\text{Nb}_2\text{O}_6 \cdot \text{H}_2\text{O}$. The precursor obtained by the MAHM after a 40 minute synthesis was identified using powder XRD (Fig. S1, ESI†) as monoclinic $\text{Na}_2\text{Nb}_2\text{O}_6 \cdot \text{H}_2\text{O}$ with space group $C12/c1$.⁵⁹ According to the diffractogram shown in Fig. 1, the conventional thermal treatment of $\text{Na}_2\text{Nb}_2\text{O}_6 \cdot \text{H}_2\text{O}$ promotes the formation of orthorhombic NaNbO_3 . The inset of the most intense peaks (I, II, and III) shows the peak overlap between the NaNbO_3 obtained and theoretical patterns, indicating that the sample might be composed of two possible orthorhombic NaNbO_3 phases: the ferroelectric phase with the $P2_1ma$ space group and the antiferroelectric phase with the $Pbcm$ space group.

To clarify the polymorphism in the sample, we performed the Rietveld refinement by combining the $P2_1ma$ and $Pbcm$ phases, and each phase individually (Fig. 2). The best statistical values and optimal curve fitting were achieved by including both $P2_1ma$ and $Pbcm$ phases in the refinement calculations, as shown in Table 1.

According to the Rietveld refinement quantitative analysis, the sample consists of 87.10 wt% of the $P2_1ma$ ferroelectric phase and 12.90 wt% of the $Pbcm$ antiferroelectric phase.

In the NaNbO_3 perovskite structure, sodium is located at the interstitial sites in the vertex of the unit cell with twelve-coordinated sodium sites, with niobium occupying the octahedral site.

Octahedral tilting is an intrinsic characteristic of perovskite structures (ABO_3) caused by the difference in the size of the A- and B-sites; in addition to the NaNbO_3 structure, A = Na^+ , and B = Nb^{5+} cations. The $[\text{BO}_6]$ tilting of the orthorhombic

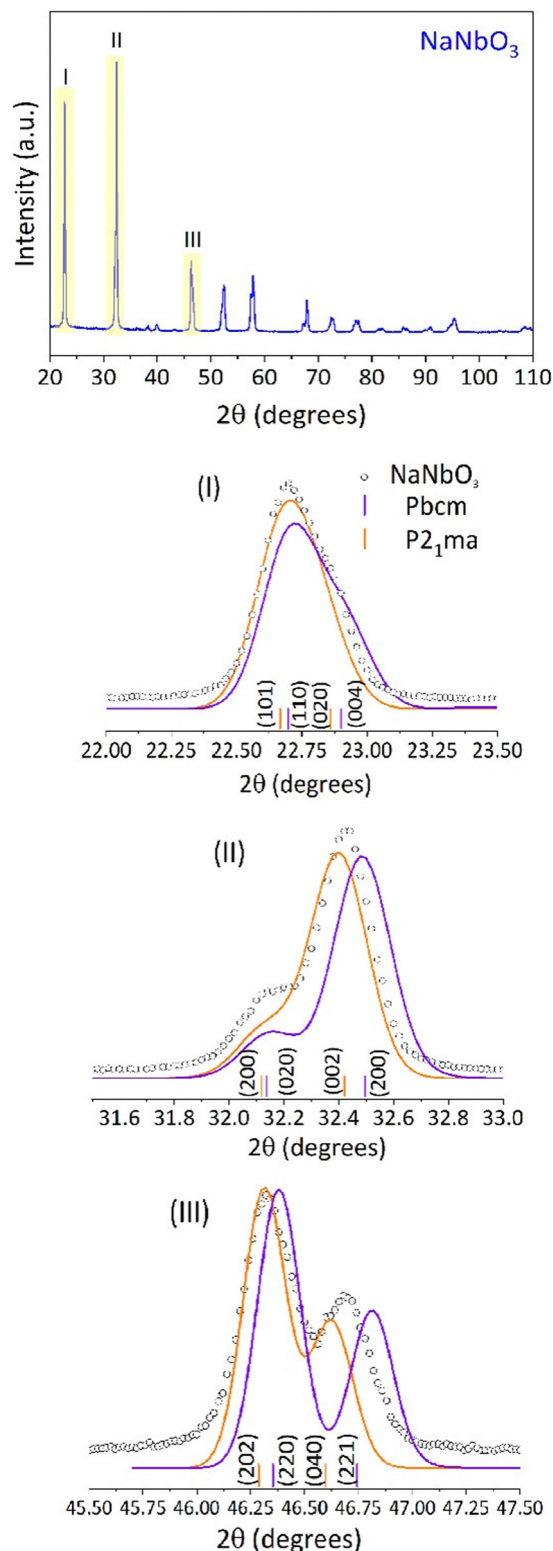


Fig. 1 X-ray diffraction of NaNbO_3 obtained after thermal treatment at 550 °C of $\text{Na}_2\text{Nb}_2\text{O}_6 \cdot \text{H}_2\text{O}$. The insets highlight the peaks at around 22 °C (I), 32 °C (II), and 46 °C (III).

perovskite structure occurs around the b and c axes.²⁴ The phase transition in NaNbO_3 has been linked to the tilting and distortion on $[\text{NbO}_6]$ octahedra and the off-centered displacement

$P2_1ma$ ferroelectric 87.10 wt%
 $Pbcm$ antiferroelectric 12.90 wt%

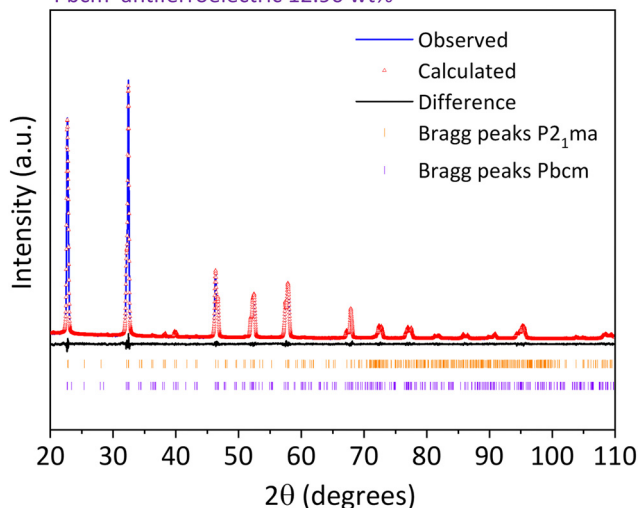


Fig. 2 Rietveld refinement of NaNbO_3 fibers.

Table 1 Statistical values obtained by Rietveld refinement

Refinement parameters	Ferroelectric phase ($P2_1ma$: CIF n° 39624)	Antiferroelectric phase ($Pbcm$: CIF n° 23239)	Ferroelectric and antiferroelectric phase
χ^2	1.40	1.43	1.11
R_{wp}	7.16	7.29	5.85
R_{exp}	5.11	5.11	5.24
R_{wp_dash}	12.10	12.31	9.09
R_{exp_dash}	8.64	8.64	8.15
d -DW	0.82	0.79	1.33
R_{Bragg}	0.71	0.90	0.39 to $P2_1ma$ 0.60 to $Pbcm$

of niobium atoms.⁶⁰ Atom positions for most phases were refined, providing considerable variations in the positions of Na1, Nb1, O1, and O2 atoms (see Tables S1 and S2, ESI†).

These variations are caused by the displacement of atoms resulting in more distortions in the $P2_1ma$ phase than in $Pbcm$.

Additionally, the Nb–O bonding distortions are more pronounced in the $P2_1ma$ structure,⁶⁰ and displacements of oxygen positions within the planes formed by Nb and O atoms increase the NbO_6 octahedra tilts more in the antiferroelectric phase than in the ferroelectric one.⁶¹ Table 2 shows the comparative results obtained from Rietveld refinement and DFT calculations. The values obtained indicate an agreement between the theoretical and experimental parameters.

The FEG-SEM micrographs of the powders synthesized (Fig. 3) show that the product obtained by the MAHM consists of fibers (Fig. 3a), and the fiber-like shape has remained after the conventional thermal treatment at 550 °C (Fig. 3b); in addition, it is evident that conventional heating reduces the length of the fibers. Since microwave radiation quickly heats the reaction medium, we produced $\text{Na}_2\text{Nb}_2\text{O}_6 \cdot \text{H}_2\text{O}$ fibers in a shorter synthesis time than the conventional hydrothermal method,¹⁶ employing PVA to ensure the growth of

Table 2 Summary of the structural parameters from Rietveld refinement and DFT calculations

	$P2_1ma$				
	Experimental		Theoretical		
	Rietveld	Literature ⁶¹	PBE	B3LYP	HSE06
Wt% phase	87.10	—	—	—	—
a [Å]	5.5651(1)	5.569	5.610	5.557	5.539
b [Å]	7.7731(2)	7.790	7.829	7.755	7.739
c [Å]	5.5098(2)	5.518	5.540	5.471	5.466
V [Å ³]	238.347 (17)	239.38	243.32	235.77	234.37
R_{Bragg}	0.39	—	—	—	—
	$Pbcm$				
	Experimental		Theoretical		
	Rietveld	Literature ⁶²	PBE	B3LYP	HSE06
Wt% phase	12.90	—	—	—	—
a [Å]	5.5147(25)	5.506	5.540	5.479	5.473
b [Å]	5.5809(19)	5.566	5.617	5.569	5.548
c [Å]	15.6511(84)	15.52	15.628	15.469	15.447
V [Å ³]	481.703(382)	475.632	486.31	472.00	469.13
R_{Bragg}	0.60	—	—	—	—

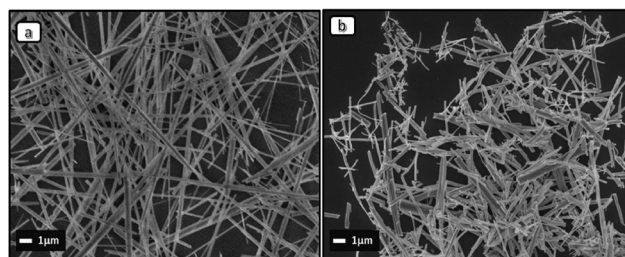


Fig. 3 FE-SEM images of (a) $\text{Na}_2\text{Nb}_2\text{O}_6 \cdot \text{H}_2\text{O}$ before thermal treatment at 550 °C for 4 hours; and (b) NaNbO_3 obtained after thermal treatment of $\text{Na}_2\text{Nb}_2\text{O}_6 \cdot \text{H}_2\text{O}$ at 550 °C.

one-dimensional morphology and avoid the formation of the isotropic NaNbO_3 .

Herein, we can consider that two types of templates influence the growth of NaNbO_3 : the polymeric template that acts to obtaining $\text{Na}_2\text{Nb}_2\text{O}_6 \cdot \text{H}_2\text{O}$, and the as-prepared $\text{Na}_2\text{Nb}_2\text{O}_6 \cdot \text{H}_2\text{O}$, working as a self-sacrificing template for the NaNbO_3 fibers to grow through conventional heating.⁶³

Higher temperatures have been reported to promote a phase transition between two centrosymmetric structures ($Pm\bar{m}a$ to $Pbcm$) passing to a non-centrosymmetric $Pmc2_1$ structure (alternative setting $P2_1ma$); in addition, the presence of each phase is also related to the particle size.^{8,9} According to Johnston *et al.*,¹⁴ the pure phase and the coexistence of the $Pbcm$ and $P2_1ma$ polymorphs are associated with the synthesis methods and their varying parameters. A mix of $Pbcm$ and $P2_1ma$ structures is obtained through the solid-state reaction and molten salt synthesis; however, regardless of the synthesis parameters, the $Pbcm$ phase was consistently present as the major phase, suggesting it to be the more thermodynamically stable of the two polymorphs. In addition, molten salt approaches allow obtaining a pure $Pbcm$ phase after a long

Table 3 Energy difference between the NaNbO_3 polymorphs

Functional	$E_{P2_1ma} - E_{Pbcm}$ (meV/f.u.)
PBE(D3-BJ)	5.8337
B3LYP(D3-BJ)	6.8644
HSE06(D3-BJ)	3.8225

heating period at 1000 °C.¹⁴ A mix of *Pbma* and *P2₁ma* structures is also obtained through hydrothermal synthesis at 200 °C for 24 hours; in addition, as in the aforementioned methods, the *Pbma* phase predominates. In this case, the *Pbma* phase is isolated by heating the as-prepared NaNbO_3 at 950 °C for 24 hours, while the pure *P2₁ma* structure is produced through thermal treatment at 600 °C for 6 hours.⁶⁰

Despite the similar thermodynamic stability of the two phases,¹⁴ the *Pbcm* structure is formed more easily. DFT simulations allow estimating the energy difference between the polymorphs (Table 3), showing that the antiferroelectric *Pbcm* phase is slightly more stable than the ferroelectric *P2₁ma* phase.

Unlike our work, in the cases reported above, NaNbO_3 was crystallized directly from the chosen synthesis method. Although the evidence showing that the *Pbcm* phase is more stable, in our work, the 4 hour thermal annealing of the metastable $\text{Na}_2\text{Nb}_2\text{O}_6 \cdot \text{H}_2\text{O}$ at 550 °C favors the formation of the *P2₁ma* structure of NaNbO_3 instead of *Pbcm*. Our results are consistent with several works that report the production of piezoelectric NaNbO_3 (*P2₁ma* phase) in one-dimensional morphology by heating a metastable phase of NaNbO_3 under similar conditions used herein^{2,15,25,64–66} since the heating at temperatures above 600 °C modifies the one-dimensional morphology and produces a monoclinic phase of NaNbO_3 .⁶⁶

In our previous work,²⁴ Rietveld refinement showed that a pure antiferroelectric phase of NaNbO_3 was obtained from the direct crystallization into solution using the MAHM.²⁴ However, in the present study, the MAHM was employed to produce $\text{Na}_2\text{Nb}_2\text{O}_6 \cdot \text{H}_2\text{O}$, and the conventional treatment of the product obtained from the MAHM promotes obtaining NaNbO_3 with the coexistence of antiferroelectric and ferroelectric structures. Besides, through this processing, the ferroelectric phase is preferably formed than the antiferroelectric, implying that somehow such phase is stabilized during the synthesis, or it is the kinetic product in such a synthesis condition.

In addition to X-ray diffraction and Rietveld refinement, Raman spectroscopy is an excellent tool for structural investigation and unveiling the short-range order since it is sensitive to the vibrations of the atoms in the crystalline structure.

The Raman spectra of the NaNbO_3 structure (Fig. 4) are composed of low-energy external and high-energy internal vibrational modes. External vibrational modes are translation modes resulting from the interaction between the NbO_6 octahedron and Na^+ cation and are responsible for a split band profile due to the presence of the Na^+ site. The interaction between NbO_6 – NbO_6 octahedra contributes to external vibrational modes. Internal vibrational modes arise from bending between O–Nb–O bonding angles and stretching of the Nb–O bonds. The variation in the geometric center of the NbO_6

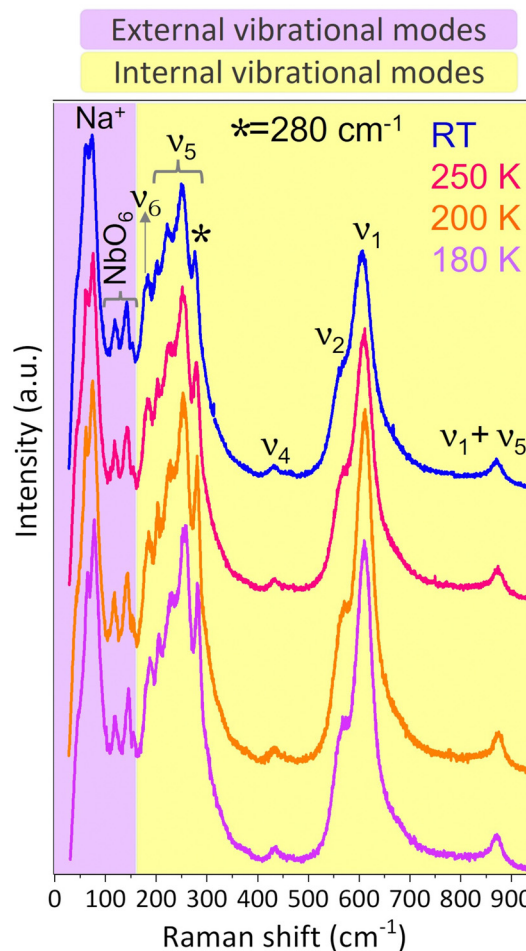


Fig. 4 Raman spectra of NaNbO_3 fibers (obtained after thermal treatment of $\text{Na}_2\text{Nb}_2\text{O}_6 \cdot \text{H}_2\text{O}$) recorded at different temperatures.

octahedron and the displacement of Na^+ cations cause tilt and distortion in the octahedron leading to the phase transition.⁶⁷

Several reports draw on Raman spectroscopy under various temperature conditions as a tool to understand the NaNbO_3 phase transition. As NaNbO_3 has an orthorhombic symmetry between -100 °C and 575 °C,⁶⁸ we performed Raman spectroscopy measurements at 180 K (~ -93 °C), 200 K (~ -73 °C), 250 K (~ -23 °C) and, at room temperature (RT). According to Jauhari *et al.*, the low temperature leads to a structural disorder resulting in the appearance, disappearance, and displacement of vibrational modes.⁶⁹ Therefore, Raman spectra were recorded to further prove the presence of both antiferroelectric and ferroelectric phases in NaNbO_3 with an orthorhombic crystalline structure.

Investigating the phase transition from *Pbcm* to *P2₁ma* structure, Lin *et al.* verified that the band intensities at 62 and 75 cm^{-1} decrease with increased temperature.⁷⁰ In work by Shiratori *et al.*, the Raman spectrum obtained for the *Pbcm* structure presents a splitting in the band located between 61 and 74 cm^{-1} ; however, no splitting is noticed for the ferroelectric phase.⁹ Shakhovoy *et al.* also relate the ferroelectric and antiferroelectric polymorphs of NaNbO_3 to the profile of the

bands at lower wavenumbers.⁷¹ Herein, the bands between 44 and 78 cm^{-1} are split (Fig. 4); moreover, the splitting profile changes as a function of temperature. The DFT calculations (Tables S3 and S4, ESI†) allow assigning the 65 cm^{-1} vibration to a B_2 mode in the $P2_1ma$ polymorph, with a DFT calculated frequency of 58 cm^{-1} and schematics shown in Fig. 5b, and the 78 cm^{-1} vibration to an A_g mode from the $Pbcm$ one, with a DFT calculated frequency of 73 cm^{-1} (shown in Fig. 5a).

According to Ji *et al.*,² the ferroelectric and antiferroelectric structures are differentiated by the splitting in the bands located in the region from 150 to 300 cm^{-1} ; furthermore, the intensity of the peak at 274 cm^{-1} is lower for the ferroelectric structure.¹⁶ This intense peak has a contribution of an A_1 mode from the $P2_1ma$ polymorph with a DFT calculated frequency of 277 cm^{-1} . In addition, the peak at 280 cm^{-1} appears to have a significant contribution from the A_g mode with a DFT calculated frequency of 291 cm^{-1} , and such a peak decreases in intensity as the temperature increases.

To better compare the bands, the intensities of the spectra obtained at room temperature and 180 K were normalized

(Fig. 6). By examining the normalized spectra, we notice that the temperature rise promotes the increase in the intensity of the peak at 65 cm^{-1} and decreases the intensity of the bands related to the Nb–O vibrations (225, 255, and 280 cm^{-1}) and the NbO_6 octahedra (560 and 609 cm^{-1}) vibrations. The spectra shown in Fig. 6 and the relative intensities obtained from the DFT calculations (Tables S3 and S4, ESI†) show the $P2_1ma$ polymorph with the most intense peak around 65 cm^{-1} without the $Pbcm$ polymorph presenting intense peaks in the same region. Thus, the $P2_1ma$ polymorph is responsible for decreasing the intensity of the bands resulting from the internal vibrational modes with the lower temperature, which, in turn, increases the structural disorder of the material and reduces the unit cell polarity.^{72,73}

In the spectra collected at 180, 200, and 250 K (Fig. 4), the band pattern located between 55 and 80 cm^{-1} is the same as those obtained by Shakhovoy *et al.*⁷¹ when analyzing regions with the coexistence of the ferroelectric and antiferroelectric phases. Therefore, based on the intensity of the bands and their respective splitting, we assume that the higher temperature

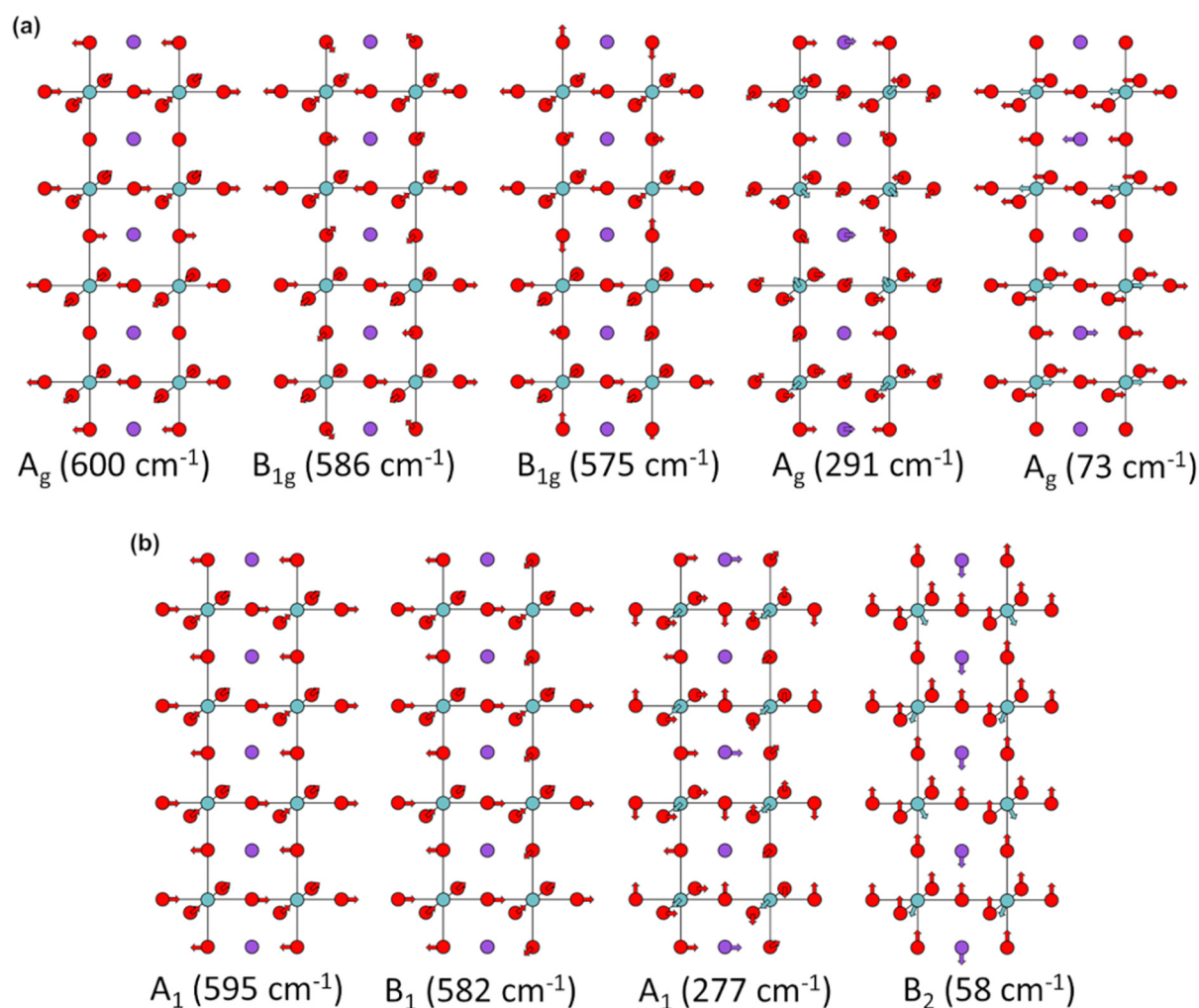


Fig. 5 Schematics of some Raman modes obtained using DFT of the (a) $Pbcm$ and (b) $P2_1ma$ space groups. Color scheme: oxygen (red), niobium (green), and sodium (purple). To ease the visualization, all the octahedral distortions were removed.

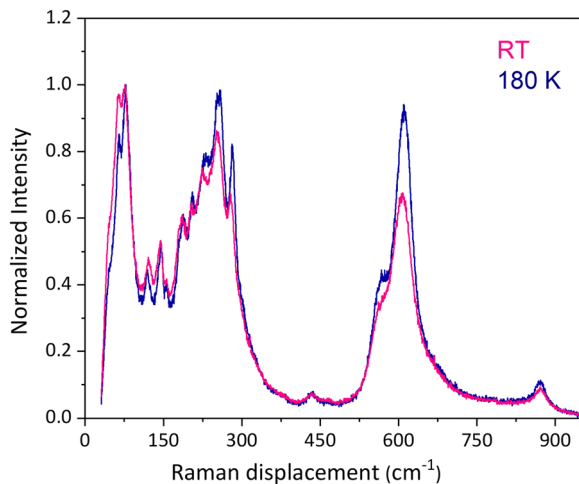


Fig. 6 Raman normalized spectra for NaNbO₃ fibers recorded at RT and 180 K.

favors the presence of a ferroelectric structure, although the ferroelectric and antiferroelectric phases coexist at all temperatures throughout the analysis.

The electric field has been reported to induce the transformation of the antiferroelectric phase into the ferroelectric phase. This phase modification occurs because the atomic displacements caused by the electric field distort the oxygen octahedrally and modify the NaNbO₃ structure.⁶¹

Based on such a behavior presented by NaNbO₃, we verified the possibility of a phase transition occurring. DFT simulations allow us to observe the effect of applying an electric field on the relative energy between the NaNbO₃ polymorphs. The Electronic Supplementary Information (ESI†) contains the complete procedure for the rotations of the standard *Pmc2₁* unit cell, the growth manner to make the atomic sites match the positions between the polymorphs, and the relationship between the applied internal electric field and the correlated macroscopic field. These calculations (Fig. S2–S4, ESI†) showed that only the electric fields in the *x* and *y* directions can invert the relative energy between the polymorphs. In addition, the electric field magnitudes needed for such inversion are approximately 6.2 MV cm⁻¹ and 14.6 MV cm⁻¹, respectively. Thus, a few orders of magnitude are more prominent than those found experimentally for a single-crystal and powder samples.^{61,74,75} Therefore, they should be observed more qualitatively than quantitatively since the literature reports a divergence between the absolute experimental and theoretical values of electric fields.⁷⁶

We employed the piezo response microscopy technique to investigate the nanoscale ferroelectric characteristics and the polarization vector of the ferroelectric domain structure of NaNbO₃ fibers. The out-of-plane (OP-PFM) and in-plane (IP-PFM) piezo response images correspond to the perpendicular (vertical) and parallel (horizontal) contributions to the fiber surface of the ferroelectric polarization vector, respectively. Fig. 8 shows the surface topography and piezo response images with a scan size of 1 μm × 1 μm. The NaNbO₃ fiber has a width of 422 nm and a

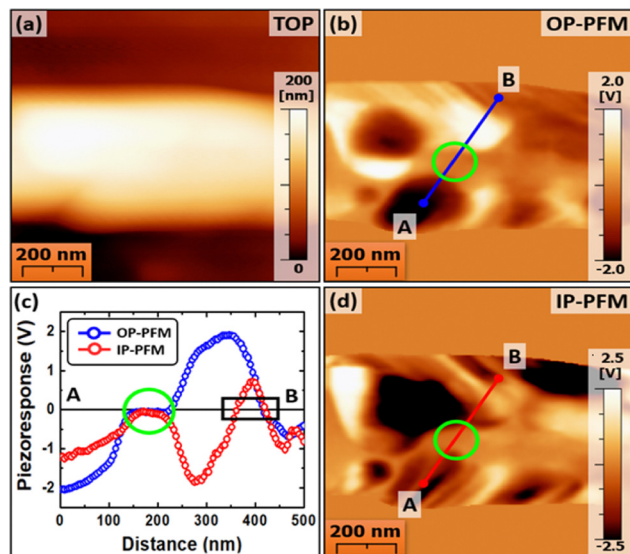


Fig. 7 NaNbO₃ fiber (a) topography, (c) piezo response signal cross-section from blue and red lines in (b) out-of-plane, and (d) in-plane piezo response images with frequencies of 50 kHz and 5 kHz, respectively.

height of 167 nm (Fig. 7a). The out-of-plane (OP-PFM at a frequency of 50 kHz, Fig. 7b) and in-plane (IP-PFM at a frequency of 5 kHz, Fig. 7d) piezo response images correspond to the same ferroelectric domain structure in the fiber surface and reveal high contrasted PFM images. The clear and dark regions of the color scale contrast represent the opposite polarization orientations in the ferroelectric domain structure. The solid lines (A and B, blue and red lines) from the cross-section as shown in Fig. 7c show the piezo response intensity. However, the results indicate that there are regions with a null piezo response signal, thus indicating regions with no ferroelectric characteristics, as highlighted by the green solid line circle.

Fig. 8 shows the following regions measured by PFM in different colors: regions of opposite orientations of the ferroelectric domains (red and blue), regions without piezo response signals (green), and regions corresponding to the substrate (black). The regions without piezo response signals were computed as 17.7% for OP-PFM and 15.8% for IP-PFM. The

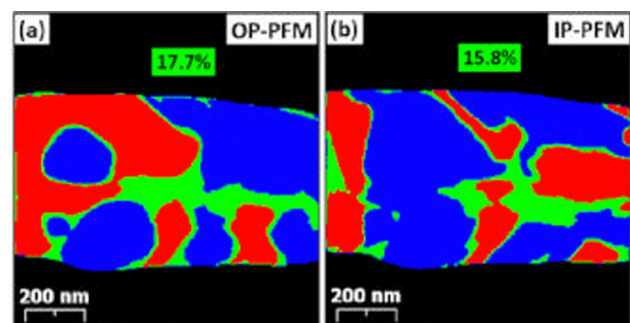


Fig. 8 Ferroelectric domain structure of the NaNbO₃ fiber: (a and b) piezo response images in distinct colors (red and blue - opposite polarization orientations, green - non-response, and black - substrate).

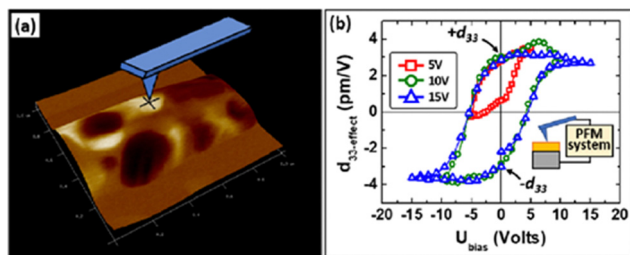


Fig. 9 Local ferroelectric switching: (a) tip position on the NaNbO_3 fiber and (b) piezo-hysteresis curves with different bias ranges.

different values occur due to the orientation of the polarization vector on the fiber surface and its contributions to the vertical and horizontal orientations.

These percentual values are higher than the value obtained from Rietveld refinement for the antiferroelectric phase (12.9 wt%). PFM generates these higher values because the domain wall regions in PFM measurements with an inverted orientation of ferroelectric domains (see the solid black rectangle in Fig. 8c) were also computed as regions of null values of piezo response signal.^{77,78}

To investigate the switching behavior of nanoscale ferroelectric domains, we performed successive measurements of the local piezo loops using electrical voltages of 5 V, 10 V, and 15 V in a region with a high magnitude of piezo response signal. Fig. 9(a) shows the position on top of the NaNbO_3 fiber where the cycles were performed. Fig. 9(b) shows that the cycle of 5 V bias did not generate an electric field superior to the coercive electric field (E_c) of the material capable of switching the ferroelectric domain locally just below the tip. However, the other cycles with a larger bias were able to reorientate the ferroelectric polarization. The peak-to-peak amplitude of the effective d_{33} coefficient obtained ($\Delta d_{33} = |+d_{33}| + |-d_{33}|$) was approximately 5.89 pm V^{-1} .

In a previous work, we reported the piezoelectric and ferroelectric effect presented by flexible composites constituted by NaNbO_3 particles with different morphologies and α -polyvinylidene difluoride (α -PVDF).⁷⁹ Since α -PVDF is a non-polar phase of PVDF,⁸⁰ we concluded that the piezoelectric and ferroelectric behaviors of the composites originate from NaNbO_3 particles. Herein, we deepen the study of the structure of NaNbO_3 fiber-like particles supported by PFM characterization to explain the piezoelectric behavior of NaNbO_3 fibers.

Conclusions

In summary, $\text{Na}_2\text{Nb}_2\text{O}_6 \cdot \text{H}_2\text{O}$ fiber-like particles were obtained at 160°C over a 40-minute synthesis through a microwave-assisted hydrothermal method in a PVA medium. The $\text{Na}_2\text{Nb}_2\text{O}_6 \cdot \text{H}_2\text{O}$ fibers were applied as a precursor to obtain anisotropic NaNbO_3 fiber-like particles. The results of powder XRD, Rietveld refinement, and Raman spectroscopy showed that the antiferroelectric ($Pbcm$) and ferroelectric phases ($P2_1ma$) coexist in the structure of the NaNbO_3 fibers. The theoretical study demonstrated that the relative stability between

the antiferroelectric and ferroelectric phases could be inverted under the influence of an electric field. Such an inversion depends on the orientation of the field PFM, whose measurements showed that an isolated fiber is composed of ferroelectric and non-ferroelectric phases. This finding, in turn, corroborates the results of the structural analysis.

Furthermore, the analysis of the theoretical results indicates that the non-ferroelectric phase may be an antiferroelectric phase. Since the piezoelectric efficiency of NaNbO_3 -based devices is linked to the structure of the ceramic structure, the characteristics of the particles reported herein reinforce the potential of NaNbO_3 for application in technologies based on the piezoelectric effect.

Author contributions

G. F. Teixeira: conceptualization, methodology, validation, formal analysis, investigation, writing – original draft. H. S. Seleghini: validation, methodology, investigation, formal analysis, writing – original draft. W. B. Bastos: validation, methodology, investigation, formal analysis, writing – original draft. N. Jacomaci: methodology, formal analysis, investigation, writing – original draft. B. Stojadinović: resources, investigation. Z. Dohčević-Mitrović: resources, investigation, supervision. F. Colmati: supervision, conceptualization, writing – original draft. M. A. San-Miguel: resources, supervision, writing – original draft. E. Longo: supervision, resources, funding acquisition. M. A. Zaghete: supervision, resources, funding acquisition, project administration. All authors have read and agreed to the submitted/published version of the manuscript.

Conflicts of interest

There are no conflicts to declare.

Acknowledgements

The authors would like to thank the Brazilian research agencies CAPES (Processes number: 88881.068060/2014-01 and 88882.306480/2018-1), FAPESP-(CEPID/CDMF 2013/07296-2, 2016/23891-6, 2017/26105-4, and 2017/10819-8) for the financial support to this research. HSS would like to thank the Brazilian National Council for Scientific and Technological Development (CNPq) for the scholarship 130518/2019-0. Z. D. M. and B. S. would like to thank the Institute of Physics Belgrade for the funding granted by the Ministry of Education, Science, and Technological Development of the Republic of Serbia. This research used the computing resources and assistance of the John David Rogers Computing Center (CCJDR) in the Institute of Physics Gleb Wataghin, University of Campinas.

Notes and references

- H. You, X. Ma, Z. Wu, L. Fei, X. Chen, J. Yang, Y. Liu, Y. Jia, H. Li, F. Wang and H. Huang, *Nano Energy*, 2018, **52**, 351–359.

- 2 S. Ji, H. Liu, Y. Sang, W. Liu, G. Yu and Y. Leng, *CrystEngComm*, 2014, **16**, 7598–7604.
- 3 S. I. Raevskaya, M. A. Malitskaya, C. C. Chou, A. G. Lutokhin, I. P. Raevski and V. V. Titov, *Phys. Status Solidi A*, 2019, **216**, 1–5.
- 4 D. Fernandes, C. W. Raubach, P. L. G. Jardim, M. L. Moreira and S. S. Cava, *Ceram. Int.*, 2020, **47**, 10185–10188.
- 5 G. F. Teixeira, T. R. Wright, D. C. Manfroi, E. Longo, J. A. Varela and M. A. Zaghete, *Mater. Lett.*, 2015, **139**, 443–446.
- 6 M. H. Prado da Silva, D. N. da Rocha, L. de Andrade Gobbo, L. M. dos Santos Azevedo, L. H. L. Louro, A. Machado Costa and J. Brant de Campos, *J. Biomed. Mater. Res., Part B*, 2016, **104**, 979–985.
- 7 Z. X. Shen, X. B. Wang, S. H. Tang, M. H. Kuok and R. Malekfar, *J. Raman Spectrosc.*, 2000, **31**, 439–443.
- 8 Y. Shiratori, A. Magrez, W. Fischer, C. Pithan and R. Waser, *J. Phys. Chem. C*, 2007, **111**, 18493–18502.
- 9 Y. Shiratori, A. Magrez, J. Dornseiffer, F. H. Haegel, C. Pithan and R. Waser, *J. Phys. Chem. B*, 2005, **109**, 20122–20130.
- 10 M. Tyunina, A. Dejneka, D. Rytz, I. Gregora, F. Borodavka, M. Vondracek and J. Honolka, *J. Phys.: Condens. Matter*, 2014, **26**, 125901.
- 11 X. B. Wang, Z. X. Shen, Z. P. Hu, L. Qin, S. H. Tang and M. H. Kuok, *J. Mol. Struct.*, 1996, **385**, 1–6.
- 12 N. Chaiyo, R. Muanghlua, S. Niemcharoen, B. Boonchom and N. Vittayakorn, *J. Alloys Compd.*, 2011, **509**, 2445–2449.
- 13 H. D. Megaw, *Ferroelectrics*, 1974, **7**, 87–89.
- 14 K. E. Johnston, C. C. Tang, J. E. Parker, K. S. Knight, P. Lightfoot and S. E. Ashbrook, *J. Am. Ceram. Soc.*, 2010, **132**, 8732–8746.
- 15 D. Zhang, F. Shi, J. Cheng, X. Yang, E. Yan and M. Cao, *Ceram. Int.*, 2014, **40**, 14279–14285.
- 16 S. Ji, H. Liu, Y. Sang, W. Liu, G. Yu and Y. Leng, *CrystEngComm*, 2014, **16**, 7598–7604.
- 17 A. Toprak and O. Tigli, *Appl. Phys. Rev.*, 2014, **1**, 031104.
- 18 S. Sharma, R. Kiran, P. Azad and R. Vaish, *Energy Convers Manage*, 2022, **254**, 115272.
- 19 Z. Yang, S. Zhou, J. Zu and D. Inman, *Joule*, 2018, **2**, 642–697.
- 20 M. Safaei, H. A. Sodano and S. R. Anton, *Smart Mater. Struct.*, 2019, **28**, 113001.
- 21 R. Zhu and Z. Whang, Piezoelectric one- to two- dimensional nanomaterials for vibration energy harvesting devices, in *Emerging 2D Materials and Devices for the Internet of Things: Information, Sensing and Energy Applications*, ed. E. Tao, D. Akinwande, Elsevier, Amsterdam, 2020. pp. 221–240.
- 22 L.-Q. Cheng and J. F. Li, *J. Materiomics*, 2016, **2**, 25–36.
- 23 G. Yang and S. J. Park, *Materials*, 2019, **12**, 1177.
- 24 G. F. Teixeira, E. Silva Junior, A. Z. Simões, E. Longo and M. A. Zaghete, *CrystEngComm*, 2017, **19**, 4378–4392.
- 25 J. H. Jung, M. Lee, J. il Hong, Y. Ding, C. Y. Chen, L. J. Chou and Z. L. Wang, *ACS Nano*, 2011, **5**, 10041–10046.
- 26 S. Wu, J. Zhang, X. Liu, S. Lv, R. Gao, W. Cai, F. Wang and C. Fu, *Nanomaterials*, 2019, **9**, 190.
- 27 C. Harnagea, M. Azodi, R. Nechache, C.-V. Cojocaru, V. Buscaglia, M. T. Buscaglia, P. Nanni, F. Rosei and A. Pignolet, *Phase Transitions*, 2013, **86**, 635–650.
- 28 C. Harnagea, A. Pignolet, M. Alexe, D. Hesse and U. Gösele, *Appl. Phys. A: Mater. Sci. Process.*, 2000, **70**, 261–267.
- 29 D. S. L. Pontes, W. B. Bastos, A. J. Chiquito, E. Longo and F. M. Pontes, *J. Alloys Compd.*, 2017, **702**, 327–337.
- 30 I. K. Bdikin, J. A. Pérez, I. Coondoo, A. M. R. Senos, P. Q. Mantas and A. L. Kholkin, *J. Appl. Phys.*, 2011, **110**, 52003.
- 31 V. V. Shvartsman, A. L. Kholkin, C. Verdier and D. C. Lupascu, *J. Appl. Phys.*, 2005, **98**, 94109.
- 32 I. K. Bdikin, A. L. Kholkin, A. N. Morozovska, S. V. Svechnikov, S.-H. Kim and S. V. Kalinin, *Appl. Phys. Lett.*, 2008, **92**, 182909.
- 33 W. B. Bastos, E. Longo, A. J. Chiquito, D. S. L. Pontes and F. M. Pontes, *Mater. Chem. Phys.*, 2018, **214**, 180–184.
- 34 L. J. McGilly, L. Feigl and N. Setter, *Thin Solid Films*, 2017, **636**, 214–219.
- 35 N. A. Pertsev, A. Petraru, H. Kohlstedt, R. Waser, I. K. Bdikin, D. Kiselev and A. L. Kholkin, *Nanotechnology*, 2008, **19**, 375703.
- 36 F. M. Pontes, A. J. Chiquito, W. B. Bastos, M. A. Pereira-da-Silva and E. Longo, *J. Mater. Chem. C*, 2016, **4**, 9331–9342.
- 37 R. A. Capeli, F. M. Pontes, A. J. Chiquito, W. B. Bastos, M. A. Pereira-da-Silva and E. Longo, *Ceram. Int.*, 2017, **43**, 5047–5052.
- 38 R. A. Capeli, F. M. Pontes, D. S. L. Pontes, A. J. Chiquito, W. B. Bastos, M. A. Pereira-da-Silva and E. Longo, *Mater. Lett.*, 2017, **196**, 64–68.
- 39 G. M. M. M. Lustosa, G. F. Teixeira, W. B. Bastos, S. M. Zanetti, L. A. Perazolli and M. A. Zaghete, *Nanosized ferroelectrics: Preparation, properties, and applications*, in *Magnetic, Ferroelectric, and Multiferroic Metal Oxides*, ed. Stojanovic B. D., Elsevier, Amsterdam, 2018. pp. 139–52.
- 40 P. Hohenberg and W. Kohn, *Phys. Rev.*, 1964, **136**, B864.
- 41 W. Kohn and L. J. Sham, *Phys. Rev.*, 1965, **140**, A1133.
- 42 R. Dovesi, A. Erba, R. Orlando, C. M. Zicovich-Wilson, B. Civalleri, L. Maschio, M. Rérat, S. Casassa, J. Baima, S. Salustro and B. Kirtman, *Wiley Interdiscip. Rev.: Comput. Mol. Sci.*, 2018, **8**, e1360.
- 43 R. Dovesi, C. Roetti, C. Freyria-Fava, M. Prencipe and V. R. Saunders, *Chem. Phys.*, 1991, **156**, 11–19.
- 44 B. Civalleri, A. M. Ferrari, M. Llunell, R. Orlando, M. Mérawa and P. Ugliengo, *Chem. Mater.*, 2003, **15**, 3996–4004.
- 45 J. Scaranto and S. Giorgianni, *J. Mol. Struct. THEOCHEM*, 2008, **858**, 72–76.
- 46 J. P. Perdew and Y. Wang, *Phys. Rev. B: Condens. Matter Mater. Phys.*, 1992, **45**, 13244–13249.
- 47 A. D. Becke, *J. Chem. Phys.*, 1993, **98**, 5648–5652.
- 48 C. Lee, W. Yang and R. G. Parr, *Phys. Rev. B: Condens. Matter Mater. Phys.*, 1988, **37**, 785–789.
- 49 J. Heyd, G. E. Scuseria and M. Ernzerhof, *J. Chem. Phys.*, 2003, **118**, 8207–8215.
- 50 A. v Krukau, O. A. Vydrov, A. F. Izmaylov and G. E. Scuseria, *J. Chem. Phys.*, 2006, **125**, 224106.
- 51 J. Heyd, G. E. Scuseria and M. Ernzerhof, *J. Chem. Phys.*, 2006, **124**, 219906.

- 52 S. Grimme, J. Antony, S. Ehrlich and H. Krieg, *J. Chem. Phys.*, 2010, **132**, 154104.
- 53 S. Grimme, S. Ehrlich and L. Goerigk, *J. Comput. Chem.*, 2011, **32**, 1456–1465.
- 54 S. Grimme, *J. Comput. Chem.*, 2006, **27**, 1787–1799.
- 55 H. J. Monkhorst and J. D. Pack, *Phys. Rev. B: Condens. Matter Mater. Phys.*, 1976, **13**, 5188.
- 56 L. Maschio, B. Kirtman, M. Rérat, R. Orlando and R. Dovesi, *J. Chem. Phys.*, 2013, **139**, 164101.
- 57 L. Maschio, B. Kirtman, M. Rérat, R. Orlando and R. Dovesi, *J. Chem. Phys.*, 2013, **139**, 164102.
- 58 C. Darrigan, M. Rérat, G. Mallia and R. Dovesi, *J. Comput. Chem.*, 2003, **24**, 1305–1312.
- 59 T. M. Nenoff, N. W. Ockwig, R. T. Cyan, T. M. Alam, K. Leung, J. D. Pless, H. Xu, M. A. Hartl and L. L. Daemen, *J. Phys. Chem. C*, 2007, **111**, 13212–13221.
- 60 G. Gouget, M. Duttine, E. Durand, A. Villesuzanne, V. Rodriguez, F. Adamietz, T. le Mercier, M.-D. Braida and A. Demourgues, *ACS Appl. Electron. Mater.*, 2019, **1**, 513–522.
- 61 V. A. Shuvaeva, M. Yu Antipin, R. S. V. Lindeman, O. E. Fesenko, V. G. Smotrakov and Yu. T. Struchkov, *Ferroelectrics*, 1993, **141**, 307–311.
- 62 A. C. Sakowski-Cowley, K. Łukaszewicz and H. D. Megaw, *Acta Crystallogr., Sect. A: Cryst. Phys., Diffr., Theor. Gen. Crystallogr.*, 1969, **25**, 851–865.
- 63 L. Liu, B. Li, D. Yu, Y. Cui, X. Zhou and W. Ding, *Chem. Commun.*, 2010, **46**, 427–429.
- 64 J. H. Jung, C.-H. Chen, W.-W. Wu, J.-I. Hong, B. K. Yun, Y. Zhou, N. Lee, W. Jo, L.-H. Chen, L.-J. Chou and Z. L. Wang, *J. Mater. Chem. C*, 2012, **116**, 22261–22265.
- 65 A. Sharma, U. Bhardwaj, D. Jain and H. S. Kushwaha, *ACS Omega*, 2022, **7**, 7595–7605.
- 66 Q. Gu, K. Zhu, J. Liu, P. Liu, Y. Cao and J. Qiu, *RSC Adv.*, 2014, **4**, 15104–15110.
- 67 S. J. Lin, D. P. Chiang, Y. F. Chen, C. H. Peng, H. T. Liu, J. K. Mei, W. S. Tse, T.-R. Tsai and H.-P. Chiang, *J. Raman Spectrosc.*, 2006, **37**, 1442–1446.
- 68 K. K. Mishra, V. Sivasubramanian and A. K. Arora, *J. Raman Spectrosc.*, 2011, **42**, 517–521.
- 69 M. Jauhari, S. K. Mishra, R. Mittal and S. L. Chaplot, *J. Raman Spectrosc.*, 2019, **50**, 1177–1185.
- 70 S. J. Lin, D. P. Chiang, Y. F. Chen, C. H. Peng, H. T. Liu, J. K. Mei, W. S. Tse, T.-R. Tsai and H.-P. Chiang, *J. Raman Spectrosc.*, 2006, **37**, 1442–1446.
- 71 R. A. Shakhovoy, S. I. Raevskaya, L. A. Shakhovaya, D. V. Suzdalev, I. P. Raevski, Y. I. Yuzyuk, A. F. Semenchov and M. el Marssi, *J. Raman Spectrosc.*, 2012, **43**, 1141–1145.
- 72 H. Qi, A. Xie, J. Fu and R. Zuo, *Acta Mater.*, 2021, **208**, 116710.
- 73 N. Sun, Y. Li, Q. Zhang and X. Hao, *J. Mater. Chem. C*, 2018, **6**, 10693–10703.
- 74 A. V. Ulinzheev, A. v Leiderman, V. G. Smotrakov, V. Y. Topolov and O. E. Fesenko, *Phys. Solid State*, 1997, **39**, 972–974.
- 75 M. H. Zhang, L. Fulanović, S. Egert, H. Ding, P. B. Groszewicz, H. J. Kleebe, L. Molina-Luna and J. Koruza, *Acta Mater.*, 2020, **200**, 127–135.
- 76 M. Harb, P. Labéguerie, I. Baraille and M. Rérat, *Phys. Rev. B: Condens. Matter Mater. Phys.*, 2009, **80**, 235131.
- 77 C.-L. Jia, S.-B. Mi, K. Urban, I. Vrejoiu, M. Alexe and D. Hesse, *Nat. Mater.*, 2008, **7**, 57–61.
- 78 L. Tian, A. Vasudevarao, A. N. Morozovska, E. A. Eliseev, S. V. Kalinin and V. Gopalan, *J. Appl. Phys.*, 2008, **104**, 74110.
- 79 G. F. Teixeira, R. A. Ciola, W. K. Sakamoto and M. A. Zaghete, *Perovskite-Based Mesostructures and Related Composites—Influence Exerted by Morphology and Interface*, in *Ferroelectric Materials-Synthesis and Characterization*, ed. Barranco A. P., IntechOpen, London, 2015, pp. 59–83.
- 80 Z. Cui, N. T. Hassankiadeh, Y. Zhuang, E. Drioli and Y. M. Lee, *Prog. Polym. Sci.*, 2015, **51**, 94–126.